

Article

MOF-Derived CeO₂ and CeZrO_x Solid Solutions: Exploring Ce Reduction through FTIR and NEXAFS Spectroscopy

Davide Salusso^{1,2}, Silvia Mauri^{3,4} , Gabriele Deplano¹ , Piero Torelli³, Silvia Bordiga¹ and Sergio Rojas-Buzo^{1,*} 

¹ Department of Chemistry, NIS Center and INSTM Reference Center, University of Turin, 10125 Turin, Italy

² European Synchrotron Radiation Facility, CS 40220, CEDEX 9, 38043 Grenoble, France

³ IOM CNR Laboratorio TASC, AREA Science Park, Basovizza, 34149 Trieste, Italy

⁴ Department of Physics, University of Trieste, Via Valerio 2, 34127 Trieste, Italy

* Correspondence: sergio.rojasbuzo@unito.it

Abstract: The development of Ce-based materials is directly dependent on the catalyst surface defects, which is caused by the calcination steps required to increase structural stability. At the same time, the evaluation of cerium's redox properties under reaction conditions is of increasing relevant importance. The synthesis of Ce-UiO-66 and CeZr-UiO-66 and their subsequent calcination are presented here as a simple and inexpensive approach for achieving homogeneous and stable CeO₂ and CeZrO_x nanocrystals. The resulting materials constitute an ideal case study to thoroughly understand cerium redox properties. The Ce³⁺/Ce⁴⁺ redox properties are investigated by H₂-TPR experiments exploited by in situ FT-IR and Ce M₅-edge AP-NEXAFS spectroscopy. In the latter case, Ce³⁺ formation is quantified using the MCR-ALS protocol. FT-IR is then presented as a high potential/easily accessible technique for extracting valuable information about the cerium oxidation state under operating conditions. The dependence of the OH stretching vibration frequency on temperature and Ce reduction is described, providing a novel tool for qualitative monitoring of surface oxygen vacancy formation. Based on the reported results, the molecular absorption coefficient of the Ce³⁺ characteristic IR transition is tentatively evaluated, thus providing a basis for future Ce³⁺ quantification through FT-IR spectroscopy. Finally, the FT-IR limitations for Ce³⁺ quantification are discussed.

Keywords: MOFs-derived oxides; Ce-UiO-66; CeZr-UiO-66; CeO₂; CeZrO_x; Ce³⁺ quantification; FT-IR; AP-NEXAFS



Citation: Salusso, D.; Mauri, S.; Deplano, G.; Torelli, P.; Bordiga, S.; Rojas-Buzo, S. MOF-Derived CeO₂ and CeZrO_x Solid Solutions: Exploring Ce Reduction through FTIR and NEXAFS Spectroscopy. *Nanomaterials* **2023**, *13*, 272. <https://doi.org/10.3390/nano13020272>

Academic Editor: Yi Huang

Received: 17 December 2022

Revised: 30 December 2022

Accepted: 5 January 2023

Published: 9 January 2023



Copyright: © 2023 by the authors. Licensee MDPI, Basel, Switzerland. This article is an open access article distributed under the terms and conditions of the Creative Commons Attribution (CC BY) license (<https://creativecommons.org/licenses/by/4.0/>).

1. Introduction

Ce-based catalysts are of great interest for their redox properties in a wide range of catalytic reactions such as CO oxidation, CO₂ hydrogenation, water-gas shift, and many more [1–10]. The catalyst surface reactivity is strongly dependent on the presence of coordinatively unsaturated sites (CUS) [11–13]. The CUS can be simply described as surface defects where the site instability provides a higher energy state, enhancing the target reaction. The CUS concentration is synthesis-dependent since high-temperature calcination treatments induce crystallite sintering and a consequent loss of defects [14]. Nevertheless, most of the investigated reactions occur at elevated temperatures or pressures, which require a certain degree of catalyst stability. The synthesis of the catalyst should therefore require a simple preparation procedure which at the same time provides a high number of defective sites which are also stable at the operating temperatures of the catalyst.

The commonly used sol-gel methods generally involve long and complex synthesis procedures [4,15–17]. On the contrary, direct precursor calcination has shown a great potential for the direct preparation of catalysts [18–22]. In the latter approach, promising results have been reported for direct calcination of metal-organic frameworks (MOFs) at

moderate temperatures (300–500 °C) [20–29]. Indeed, depending on the employed linkers, MOF synthesis can be very simple and cheap [30]. Furthermore, the natural separation of the oxide-based clusters by organic ligands prevents crystals from sintering even at high calcination temperatures, thus preserving the surface defects of the catalysts. It is noteworthy that Ce-based MOFs were recently studied as replacements for oxides in several chemical reactions [31–33]. However, the MOFs' stability still limits their practical applications [34,35]. For this reason, MOF calcination is still preferred for preparation of stable nanocatalysts. Considering Ce-based oxides, while CUS reduce the activation energy of the reaction, the key catalytic redox role is usually played by $\text{Ce}^{3+/4+}$ interconversions [1,2,12,13]. For this reason, tracking the cerium oxidation state is of major interest for understanding catalytic mechanisms. The oxidation state of cerium is often monitored by electron paramagnetic resonance (EPR) or X-ray-based techniques such as photoelectron spectroscopy (XPS), absorption spectroscopy (XAS) and near-edge absorption fine structure (NEXAFS) [36–40]. However, from a catalytic viewpoint, only XAS spectra collected with hard X-rays at Ce K- or L_3 -edges can access $\text{Ce}^{3+}/\text{Ce}^{4+}$ ratios under high temperature and pressure conditions. Unfortunately, these measurements are limited to synchrotron sources, which limits their availability. However, the presence of Ce^{3+} can also be identified with the less expensive/more available infrared spectroscopy. Indeed, it is well known that the Ce^{3+} 4f ground state splits into doublet $^2F_{5/2}$ and $^2F_{7/2}$ energy levels. They are separated by about 2000 cm^{-1} and the $^2F_{5/2} \rightarrow ^2F_{7/2}$ electronic transition is observed in the infrared range at 2127 cm^{-1} [14,41–46]. The presence/absence of this absorption band was then related to the occurrence of Ce^{3+} and it has been recently used to qualitatively monitor cerium reduction in a NiCeO_2 sample [18]. From the infrared viewpoint, the hydroxyl stretching vibration could also be used to selectively monitor Ce^{3+} formation on the catalyst surface. In fact, the $\nu(\text{OH})$ position ($\approx 3600\text{ cm}^{-1}$) depends on the hydroxyl-cation bond order, which is directly affected by Ce oxidation state, i.e., Ce^{3+} increases the bond order, causing a hypsochromic shift of the vibration [47]. The $\nu(\text{OH})$ frequency can then be used to identify the formation of $\text{Ce}^{3+}\text{-V}_\text{O}$ sites on the catalyst first surface layer, which is inaccessible to any other X-ray techniques as it represents a penetration depth of at least few nm. The use of infrared spectroscopy to safely monitor cerium's oxidation state would then provide an incredible boost to redox mechanism evaluation since FT-IR and DRIFT cells capable of operating under several thermochemical conditions are now available [48–50].

In this work, we have then prepared three MOF samples with the UiO-66 structure and different Ce:Zr ratios on the clusters, i.e., 100% Ce, 50:50 Ce:Zr and 5:95 Ce:Zr. The three samples were calcined under aerobic conditions at 450 °C to obtain three stable and defective oxides containing the respective Ce:Zr ratio. FT-IR spectra of the three CeO_2 and CeZrO_x derived-oxides were recorded during temperature programmed oxidation/reduction experiments to monitor $\nu(\text{OH})$ and Ce^{3+} infrared bands. Moreover, to compare and quantify Ce^{3+} evolution, the same experiment was repeated with an ambient pressure NEXAFS set-up. Ce M_5 -edge NEXAFS spectra were recorded under in situ conditions and Ce^{3+} was quantified through MCR-ALS routine. Ce^{3+} quantification was then combined with Ce^{3+} IR absorbance to determine its infrared molar absorption coefficient.

2. Materials and Methods

2.1. Samples Preparation

The MOF syntheses were carried out following a procedure described in the literature [51]. The corresponding amounts of aqueous solutions of cerium(IV) ammonium nitrate (Sigma-Aldrich, $\geq 99.99\%$) and/or zirconium(IV) dinitrate oxide hydrate (Sigma-Aldrich, 99%) (0.53 M) were added to a Pyrex reactor containing terephthalic acid (Sigma-Aldrich, 98%) (260 mg) and N,N-dimethylformamide (DMF) (VWR Chemicals, $\geq 99.8\%$) (see Table S1). Finally, and only in the case of Ce/Zr-UiO-66 materials, a known amount of formic acid (Sigma-Aldrich, 98%) (2.07 mL) was employed as a modulator. The resulting mixtures were magnetically stirred at 100 °C for 15 min. Then, the glass vessel reactors were cooled to RT and the reaction medium was collected by centrifugation. Finally, the MOFs

were washed three times with DMF and twice with acetone. The as-obtained materials were allowed to dry at RT overnight prior to the analyses.

The MOF-derived materials were obtained by a thermal treatment under aerobic conditions. The corresponding amount of the MOF (Table S2) was calcined up to 450 °C with a ramp of 5 °C/min with a total flow of 0.5 mL/min (air). This temperature was maintained for 4 h to completely remove the organic components.

2.2. Thermogravimetric (TG) Analysis

The TG profile was collected with a TA Instruments Q600 thermobalance under an air flow (100 mL/min) with a ramp of 5 °C/min from RT to 600 °C with about 5 mg of sample in an alumina crucible.

2.3. Powder X-ray Diffraction (PXRD)

PXRD patterns were collected with a Panalytical X-Pert diffractometer in the 3–50° and 10–100° 2 θ range for UiO-66 and oxides samples, respectively. The crystallite size was extracted through peak shape refinement using Thompson–Cox–Hastings (TCH) function implemented in FullProf software [52,53].

2.4. Specific Surface Area (SSA)

SSA was determined by applying the Brunauer–Emmett–Teller (BET) equation to N₂ adsorption/desorption isotherms collected at 77 K obtained with a Micromeritics ASAP 2020 physisorption analyzer. The samples were previously evacuated at 120 °C (for the UiO-66 samples) and 400 °C (for oxides).

2.5. Transmission Electron Microscopy (TEM)

TEM was exploited to obtain morphological and structural information of the samples. The analyses were carried out by using a TEM Jeol JEM 3010 UHR (300 kV, LaB₆ filament) equipped with X-ray EDS analysis by a Link ISIS 200 detector. The samples, in the form of powders, were deposited on a Cu grid coated with a porous carbon film.

2.6. In Situ Fourier Transform-Infrared (FT-IR)

FT-IR spectra were collected with an Aabspec cell suitable for thermal treatments under gas flows. The cell was mounted in a Bruker Invenio R spectrophotometer. Spectra were collected in transmission mode in the 4000–500 cm⁻¹ range with 2 cm⁻¹ resolution. CeO₂ was pressed in a self-supported pellet of area \approx 10 cm². The pellet was held in a gold envelope and placed in the cell sample holder. The measurement protocol (Figure S1) consisted of two parts: (I) The CeO₂ surface was cleaned from adsorbed species (H₂O, carbonates, etc.) by heating the pellet from RT to 400 °C (5 °C/min) under 50 mL/min of N₂ (99.9999%):O₂ (99.9999%) (1:1) stream. The temperature was then held at 400 °C for 60 minutes and then cooled to RT. To prevent self-reduction, the oxidising gas mixture was maintained until 150 °C, while from 150 °C to RT, the gas stream consisted of pure N₂ only. (II) Depending on the performed temperature programmed oxidation (TPO, Figure S1a) or reduction (TPR, Figure S1b) experiment (i.e., O₂-TPO or H₂-TPR, respectively), the gas mixture was replaced with a N₂:O₂ (99.9999%) or N₂:H₂ stream at 25 °C and held for 15'. After that, the TPO or TPR experiment was performed by heating the pellet from RT to 300 °C at 5 °C/min rate with a final holding at 300 °C for 30'. Both measurements were performed on the same pellet to guarantee experimental reproducibility.

2.7. Ambient Pressure Near-Edge X-ray Absorption Spectra (AP-NEXAFS)

AP-NEXAFS spectra were measured at APE-HE beamline of the Elettra Italian Synchrotron radiation source. CeO₂ was placed in a specially designed reactor cell allowing thermal treatments in the RT–400 °C range under a gas atmosphere of 1 bar. The total electron yield (TEY) mode was used to record the experimental spectra. Ce M₅-edge spectra were collected from 880 to 910 eV with 0.01 eV energy resolution. The measure-

ment protocol followed the same steps as described for the in situ FTIR measurements (Figure S1) with N₂ replaced by He (99.99999%) and with the maximum temperature limited to 350 °C. Spectra were energy aligned to a reference CeO₂ measured simultaneously with the MOF-derived material. Spectra were background subtracted and energy aligned with the Thorondor software [54]. A 6th order polynomial was used for background subtraction. Ce³⁺/Ce⁴⁺ spectral pure components and their concentration evolution were extracted using MCR-ALS implemented in MATLAB. The MCR-ALS protocol lead to lack of fit (LOF) of 3.9% with PCA and 6.2% with experimental spectra, with 99.6% of variance explained [55]. Spectra and concentration were constrained to positive values while the closure condition was applied to concentrations. Notably, to increase the variance between spectra, the H₂-TPR was conducted until 350 °C to improve Ce⁴⁺/Ce³⁺ spectra separation. Moreover, to guarantee reproducibility of the MCR-ALS protocol for the three samples, the collected spectra were analysed together in the same dataset. Ten replicas of CeO₂ and CeF₃ reference spectra were added at the end of the dataset to support the MCR-ALS protocol in finding Ce⁴⁺ and Ce³⁺ pure spectra components.

3. Results and Discussion

Ce-UiO-66 and CeZr-UiO-66 were synthesized following the procedure described by Lammert et al. [56] and reported in Materials and Methods section. The resulting solids showed the *fcu* topology characteristic of the UiO-66 materials (Figure 1a), as it can be deduced from the PXRD patterns reported in Figure 1b and Figure S2a. The PXRD patterns also presented a shift in Bragg reflections towards higher 2θ values with Zr concentration (Figure S2b), in line with the smaller ionic radii of Zr⁴⁺ (0.84 vs. 0.97 Å of Ce⁴⁺) [57]. On the other hand, the N₂ adsorption isotherms revealed the microporous nature of these MOFs. The evaluated SSA was 1000–1440 m²/g, in line with the values reported in the literature (Figure S4 and Table S3) [56]. Thermogravimetric (TG) analysis (Figure 1a) showed ~40% of weight loss in the 300–500 °C temperature range, which corresponded to the degradation of the organic linker and the subsequent transformation of the MOFs into the metal oxide. The increase in the onset temperature with the Zr content was related to the known higher stability of pure Zr-UiO-66 [58]. MOF calcination was then conducted at 450 °C to eliminate the organic components, in line with the temperatures range reported in the literature [26–29]. C100-UiO-66 calcination could have been conducted at lower temperature (≈350 °C); however, this would have induced an inhomogeneity in the samples' thermal treatments. In fact, all the successive measurements applied heating steps up to 400 °C. The calcination of the three MOFs at 450 °C then guaranteed the derived-oxides' stability within the RT–400 °C temperature range. The PXRD pattern of the obtained yellowish powder (Figure 1c) presented Bragg peaks ascribable to a cubic (Fm-3m) CeO₂ phase (JCPDS file number 34–394). As for the initial MOFs, Bragg reflections shifted to higher 2θ values with Zr concentration, in line with the Zr⁴⁺/Ce⁴⁺ ionic radii differences (Figure S2c,d). TEM images (Figure 1a,d) and crystallite size determined by PXRD Rietveld refinement (Figure S3, Table S3) confirmed that particles of among 5–10 nm were well defined and not agglomerated. An EDX analysis (Figure 1d) unveiled that the obtained oxides maintained the MOF composition, i.e., C100 (pure CeO₂), C50Z50 (Ce:Zr 49:51 wt%), and C5Z95 (Ce:Zr 5:95 wt%) with an homogeneous distribution of Ce and Zr on the surface of the samples, confirming solid solution formation. The obtained oxides presented a significant drop in SSA (Table S3), in line with the collapse of the UiO-66 structure. Moreover, hysteresis necks (Figures 1e and S4) were not observed in any of the samples. This indicated the absence of interparticle porosity, which is in line with the non-agglomerated particles observed by microscopy results.

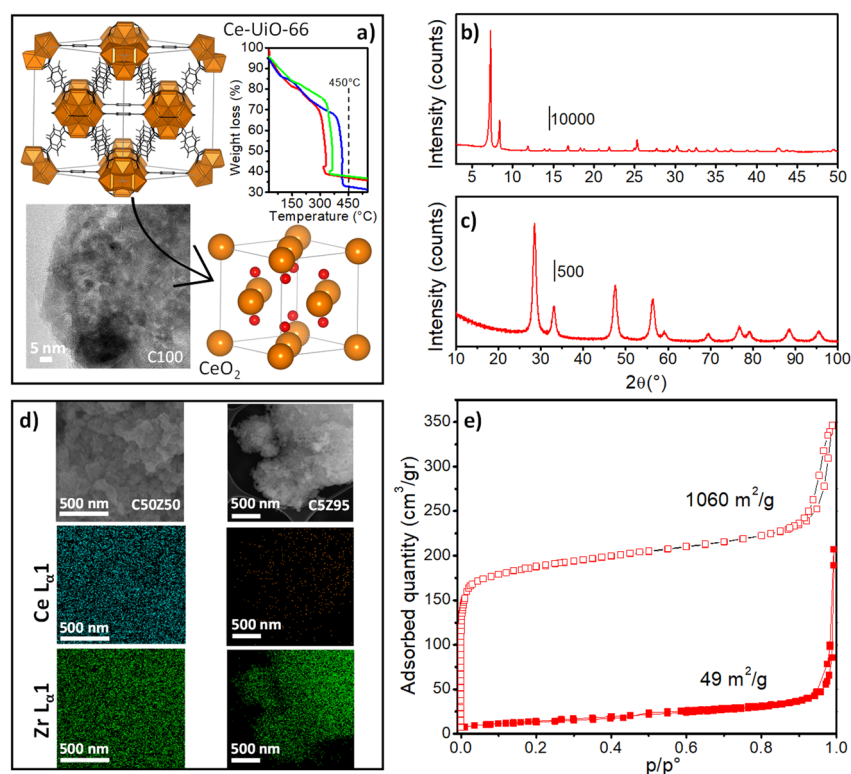
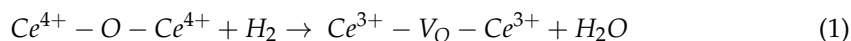


Figure 1. (a) Reported Ce-Uio-66 and CeO₂ structures (Ce atoms/clusters in orange, O in red). TG analysis of C100-(red line), C50Z50-(green line), and C5Z95-Uio-66 (blue line) are shown in the top inset. The C100 TEM image is shown in the bottom inset. The PXRD pattern of (b) C100-Uio-66 and (c) C100 samples. (d) C50Z50 and C5Z95 TEM images and EDX maps. (e) N₂ adsorption–desorption isotherms collected at 77 K over C100-Uio-66 (empty squares) and C100 (full squares) samples.

To obtain the best achievable information on the Ce oxidation state through FT-IR spectroscopy, O₂-TPO and H₂-TPR were collected over previously activated C100, C50Z50, and C5Z95 samples. The sample activation was conducted following the protocol described in the experimental section with the aim of cleaning its surface from adsorbate species (i.e., H₂O, carbonates, and organic compounds). While the O₂-TPO experiment was conducted to have a reference spectrum of oxidised CeO₂ at the different temperatures, the H₂-TPR experiment was expected to introduce Ce³⁺ and oxygen vacancies (V_O) into the sample. Indeed, as reported in Equation (1), the exposure of Ce⁴⁺-O-Ce⁴⁺ sites to H₂ at high temperatures can cause a redox reaction leading to cerium reduction and water formation.



Even though CeO₂ and CeZrO_x infrared spectra have been known for decades, we here aim to show how to exploit spectral fingerprints related to the Ce oxidation state. C100 spectra collected after thermal activation (described in SI) presented three bands in the ν(OH) region (Figure S5') at 3704, 3684, and 3657 cm⁻¹ ascribed to monodentate (m-OH), bidentate (b-OH), and tridentate (t-OH) hydroxyl groups (Figure S6), respectively. After the thermal activation, O₂-TPO was conducted (Figure 2a) to track the reference variation in ν(OH) positions with temperature. During heating under O₂, the absorbance of m- and b-OH bands decreased until a single broad band centered at 3696 cm⁻¹ was formed. At the same time, the broad band centered at ~3500 cm⁻¹, related to physisorbed water, decreased in intensity. In contrast, the t-OH lost intensity and its position shifted linearly to lower wavenumbers, (Figure 2b, red line) until it was stabilized when T = 300 °C. The band position bathochromic linear shift is associated with crystal lattice expansion. Instead, the loss of band integrated area could be related to either a decrease in surface OH groups

(i.e., sample dehydration) or to a temperature dependence of the OH molar absorption coefficient (ϵ) [59,60]. Indeed, following the Beer–Lambert Law (Equation (2)), a variation in ϵ would directly affect the integrated band area. However, this can be excluded since surface dehydration was observed from the corresponding decrease in the broad band at 3500 cm^{-1} . After having determined the spectral behavior under heating conditions, H_2 -TPR was conducted on the activated catalyst. First of all, by observing the physisorbed water band ($\sim 3500\text{ cm}^{-1}$), we noticed that the band intensity was relatively higher than the first spectra of the O_2 -TPO experiment. During H_2 -TPR, the band intensity initially decreased, indicating water desorption, while it increased again at higher temperatures. Water formation under $\text{H}_2/300\text{ }^\circ\text{C}$ is the first evidence of cerium reduction with parallel formation of oxygen vacancies (V_{O}), as described in Equation (1).

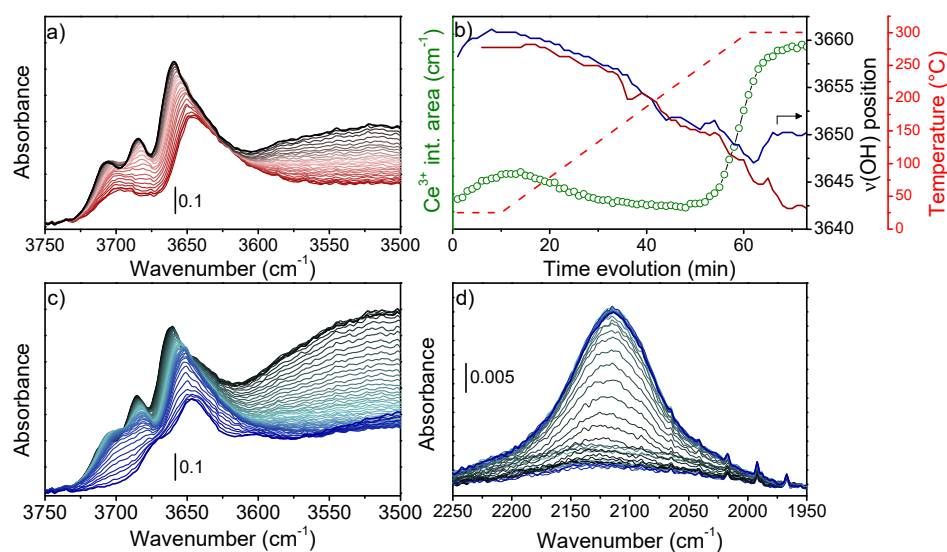


Figure 2. (a) Detail of FT-IR spectra $\nu(\text{OH})$ region collected during the O_2 -TPO experiment (temperature rise is shown as from black to red). (b) Position of t-OH maximum during H_2 -TPR (blue line) and O_2 -TPO (red line) experiments compared with Ce^{3+} band integrated area (green circles) observed during the H_2 -TPR experiment. The temperature profile is reported with a dashed red line. Detail of FT-IR spectra (c) $\nu(\text{OH})$ and (d) $\text{Ce}^{3+} {}^2\text{F}_{5/2} \rightarrow {}^2\text{F}_{7/2}$ regions (baseline corrected) collected during H_2 -TPR experiments (temperature rise is shown as from black to blue).

Moreover, the higher intensity of the band in the spectra under H_2/RT conditions suggested that surface reduction had already started at RT.

Considering the Ce-OH groups, m-OH and b-OH were rapidly consumed, whilst the t-OH band underwent a non-linear bathochromic shift (Figure 2c). Since t-OH presented a higher stability during thermal treatment, we focused on its band maximum position (Figure 2b, blue line). In particular, we observed that: (I) the frequency increased from 3658 cm^{-1} to 3661 cm^{-1} at $T = 25\text{ }^\circ\text{C}$ when the gas environment changed from N_2 to $\text{N}_2:\text{H}_2$ (see protocol Figure S1). (II) The frequency decreased when the temperature increased to $300\text{ }^\circ\text{C}$, in line with lattice expansion, and (III) the frequency shifted to 3650 cm^{-1} (8 cm^{-1} higher than the final position reached under O_2 , i.e., 3542 cm^{-1}) as soon as the temperature was stabilized at $300\text{ }^\circ\text{C}$. The origin of the t-OH shift under H_2 can be further understood from the $\text{Ce}^{3+} {}^2\text{F}_{5/2} \rightarrow {}^2\text{F}_{7/2}$ electronic transition occurring at 2127 cm^{-1} . Indeed, while this band was not observed under O_2 (Figure S5b''), it presented a relevant intensity under H_2 (Figure 2d). To understand the t-OH hypsochromic shift, it should be considered that during cerium reduction, $\text{Ce}^{3+}\text{-}V_{\text{O}}\text{-Ce}^{3+}$ sites are formed (Equation (1)). The t-OH can then arrange over the $\text{Ce}^{3+}\text{-}V_{\text{O}}\text{-Ce}^{3+}$ site, formally becoming a t'-OH group (Figure S6). Ce^{3+} increases the hydroxyl bond order causing a hypsochromic shift of the t'-OH vibration [47]. Furthermore, the Ce^{3+} integrated band absorbance intensity reported in Figure 2b (green circles) followed the same trend as the t-OH hypsochromic shift. In fact, the Ce^{3+} area (I)

increased when H₂ was added to the gas environment at a constant temperature of 25 °C, (II) it decreased during heating, and (III) it rose dramatically at T > 250 °C. This confirms the relationship between Ce³⁺ content and t-OH shift. A direct comparison of t-OH position with Ce³⁺ area gave a complete (non-quantitative) view of Ce³⁺-V_O formation on both the catalyst surface ($\nu(\text{OH})$) and in the bulk (Ce³⁺ band). Notably, the H₂O, $\nu(\text{t-OH})$ or Ce³⁺ band area which highlights surface cerium reduction under H₂, showed that the reaction had already begun at RT. This is in line with cerium's higher reducibility in the case of MOF-derived CeO₂ samples [26–29].

Nevertheless, the amount of available information extractable from FTIR spectra decreased in the case of CeZrO_x solid solutions, i.e., C50Z50 and C5Z95. In the former, the even distribution of Ce/Zr within the lattice increased the hydroxyl species population with potential similar vibrational frequencies (see Figure S6). This caused a broadening of the observed band which prevented a precise evaluation of the t-OH shift reported in Figure S7a. On the contrary, in the C5Z95 sample, the lower Ce content reduced the broadening of the OH band. This allowed observation of the same behavior noticed for C100, i.e., m-OH was consumed, b-OH was preserved, and t-OH presented a non-linear bathochromic shift. Moreover, the maximum position of the latter presented an hypsochromic shift at T ≈ 150 °C, prevailing over the lattice expansion-induced bathochromic shift (Figure S7f). As showed by NEXAFS measurements (see discussion hereafter), C5Z95-ox already contained Ce³⁺. This indicated that at 150 °C, the Ce³⁺-V_O surface concentration was sufficiently high to induce the observed shift. Concerning the Ce³⁺ 2F_{5/2} → 2F_{7/2} band, the higher Ce content in the C50Z50 sample allowed observation of the band formation (Figure S7b) which highlighted that Ce⁴⁺ reduction began at around 250 °C (Figure S7c). On the contrary, in C5Z95, the low Ce content did not allow observation of the band (Figure S7e).

To quantify cerium reduction, Ce M₅-edge AP-NEXAFS spectra were collected under the same conditions employed for the IR experiment, i.e., H₂-TPR was performed after having heated the sample for 30 minutes at 300 °C under O₂:He. Starting with C100, the as-prepared material presented a spectrum (Figure 3a) comparable to reference CeO₂ (Figure 3b inset). However, during heating under He:H₂ (Figure S8a), the Ce⁴⁺ bands initially gained intensity and lost the shoulder at 891 eV. The presence of this shoulder suggested a minor contribution of Ce³⁺ in C100 after oxidation. At T > 200 °C, the main edge lost intensity again, while a two-band shoulder arose at around 891 eV. These bands became structured around 300 °C, and at 350 °C they had a final shape clearly attributable to Ce³⁺. As we recently reported, Ce³⁺/Ce⁴⁺ can be quantified from M₅-edge NEXAFS spectra with a driven MCR-ALS protocol where 10 replicas of CeO₂ and CeF₃ references spectra are added at the end of the dataset [40]. This method allowed to improve the identification of principal components whilst simultaneously adapting the references to the dataset. The procedure identified two principal components (Figure 3b) describing 99.6% of the variance. The component spectra were clearly related to the pure spectra of Ce⁴⁺ and Ce³⁺, though with a band width specifically related to these samples. Moreover, the CeO₂ concentration profiles reported in Figure 3c indicated an evolution very close to the one observed in FT-IR experiments. We noticed that a minor content of Ce³⁺ (≈8%) was already present in the sample after oxidation which completely disappeared during heating. Ce³⁺ was then formed again at T > 200 °C and it reached levels of 10% and 30% at 300 °C and 350 °C, respectively. Even though the initial 8% of Ce³⁺ is within the MCR-ALS protocol error, we clearly observed that Ce³⁺ fingerprints were already present in C100 at RT (Figure S8b), confirming the reliability of the performed quantification.

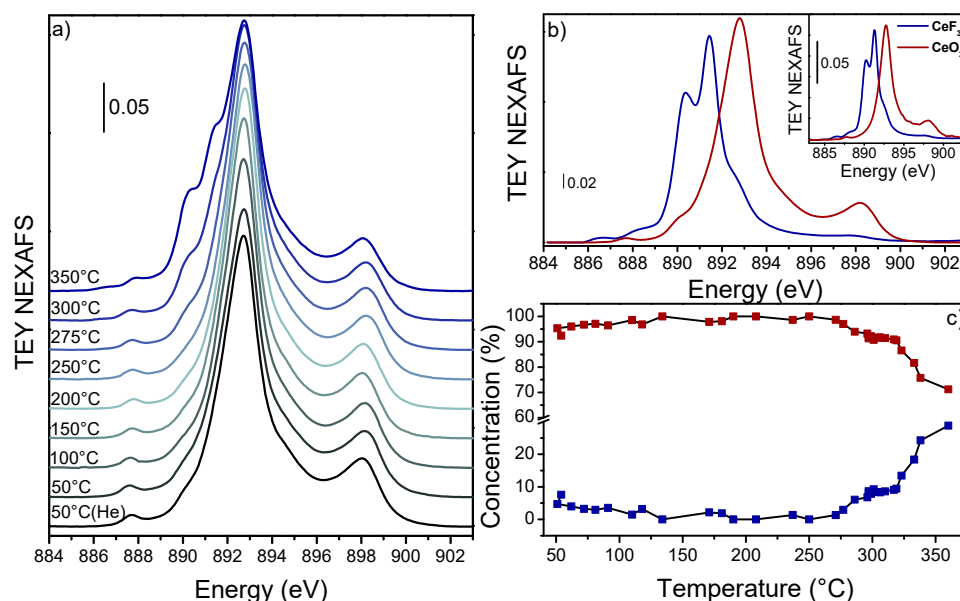


Figure 3. (a) C100 Ce M₅-edge experimental NEXAFS spectra collected under 50 mL/min H₂:He (3:2) from RT (black line) to 350 °C (blue line). The full spectra dataset is reported in Figure S4a. Ce⁴⁺ (red line/squares) and Ce³⁺ (blue line/squares) (b) spectral component and (c) concentration profiles extracted from unbiased MCR-ALS routine (99.6% of variance explained). CeO₂ and CeF₃ reference spectra are reported in the top inset with red and blue lines, respectively.

Interestingly, since the FT-IR absorbance of the Ce³⁺ band and Ce M₅-edge NEXAFS results followed the same trend, we attempted to extract the Ce³⁺ ²F_{5/2} → ²F_{7/2} transition molar attenuation coefficient. By exploiting the integrated Beer–Lambert law [61] (Equation (2) where *A* = absorbance, ϵ = molar attenuation coefficient, *c* = Ce³⁺ concentration, *w* = Ce content, and *S* = pellet area), we reported for the same temperature the evaluated Ce³⁺ concentration (through Ce M₅-edge fit) with respect to the Ce³⁺ FT-IR band integrated area (Figure S9).

$$A \left(\text{cm}^{-1} \right) = \epsilon \left(\frac{\text{cm}}{\mu\text{mol}_{\text{Ce}}} \right) * c \left(\text{wt}\% \text{ Ce}^{3+} \right) * \frac{w \left(\mu\text{mol}_{\text{Ce}} \right)}{S \left(\text{cm}^2 \right)} \quad (2)$$

The slope of the scatter plot linear fit (Figure S9) indicated that $\epsilon = 0.39 \pm 0.02 \text{ cm} / \mu\text{mol}_{\text{Ce}}$. This approach is conventionally used for determining ϵ of adsorbed species [62–65]. In contrast, this is so far the first attempt to evaluate the Ce³⁺ molar extinction coefficient and it could potentially be used in the future to evaluate Ce³⁺ concentration from FT-IR measurements.

Regarding the mixed oxides, cerium showed a higher reducibility to Ce³⁺ with an increase in Zr content. In particular, we noticed that C50Z50 and C5Z95 presented 5 and 18% of Ce³⁺ in the prepared sample, respectively. At 350 °C under H₂, the Ce³⁺ content increased to 40% for C50Z50 and 60% for C5Z95 (Figure 4). Indeed, it is well known that Ce reducibility increases in CeZrO_x solid solutions due to lattice straining induced by the different ionic radius of Zr [1,66].

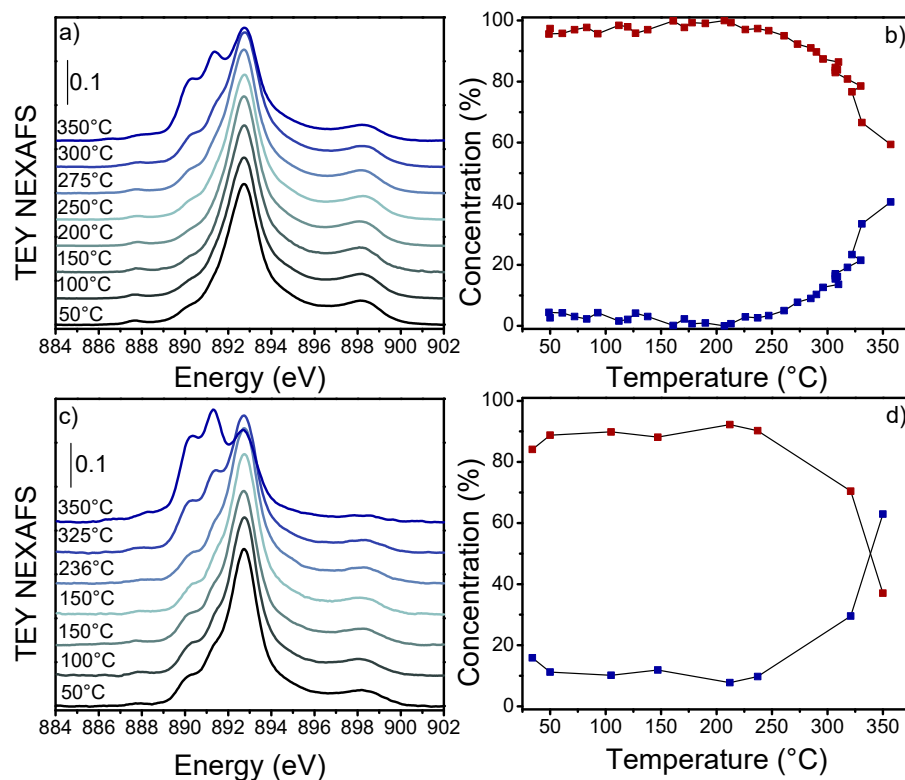


Figure 4. (a) C50Z50 and (c) C5Z95 Ce M₅-edge NEXAFS spectra measured during heating under 50 mL/min H₂:He (3:2) from RT (black line) to 350 °C (blue line). The full spectra dataset is reported in Figure S10. (b) C50Z50 and (d) C5Z95 concentration profiles of Ce⁴⁺ (red squares) and Ce³⁺ (blue squares) obtained from MCR-ALS protocol applied to the experimental spectra in panels (a,c). CeO₂ and CeF₃ reference spectra are reported (Figure 3b).

It is noteworthy that the latter sample contained $\approx 18\%$ of Ce³⁺ at 150 °C, confirming that the significant t-OH hypsochromic shift (Figure S7f) observed at this temperature was related to the high Ce³⁺ content (Figure 4c). Moreover, by combining the calculated ϵ with C50Z50 integrated absorbance after H₂-TPR at 300 °C ($\approx 1.09 \text{ cm}^{-1}$, Figure S7c), we calculated a Ce³⁺ $\approx 14\%$, in agreement with the 13.6% of Ce³⁺ evaluated from the Ce M₅-edge NEXAFS at the same temperature (Figure 4b).

4. Conclusions

Ce/Zr-UiO-66 calcination was presented as a cheap and simple synthesis pathway to obtain nanoparticles of CeO₂ and homogeneous CeZrO_x solid solutions. The MOF calcination temperature was determined by TG analysis whilst PXRD and EDX measurements confirmed a Ce/Zr homogenous dispersion. Due to their nanosize and homogeneity, the obtained oxides are ideal candidates for a deep understanding of their FTIR and NEXAFS spectra properties under reducing conditions. Cerium reduction occurred at RT under H₂ and it was related to the use of a MOF as a precursor. Moreover, Ce reducibility increased with the Zr content. A careful analysis of CeO₂ FT-IR H₂-TPR spectra unveiled that the Ce³⁺ ${}^2F_{5/2} \rightarrow {}^2F_{7/2}$ transition can be used to monitor CeO₂ bulk reduction. Moreover, we reported that the $\nu(\text{OH})$ hypsochromic shift can be used to qualitatively determine the absence/presence of Ce³⁺-V_O sites on the catalyst surface. Ce³⁺ was quantified by applying the MCR-ALS protocol to in situ Ce M₅-edge NEXAFS spectra. NEXAFS results reproduced the infrared results, hence confirming the reliability of the latter.

Eventually, by combining CeO₂ FTIR and Ce M₅-edge NEXAFS spectra, the Ce³⁺ ${}^2F_{5/2} \rightarrow {}^2F_{7/2}$ molar absorption coefficient was calculated. The coefficient was further used to calculate Ce³⁺ content in mixed CeZrO_x, leading to results in line with Ce M₅-edge NEXAFS

quantification. This proved that the determined molar absorption coefficient value could be further employed for Ce^{3+} quantification during operational FT-IR experiments.

We then demonstrated that the CeO_2 FTIR spectrum presents excellent markers to extract valuable information on the reduction state of bulk and surface Ce^{3+} . These fingerprints can be potentially monitored under relevant reaction conditions with a time resolution an order of magnitude faster than NEXAFS (seconds vs. minutes).

Nevertheless, the integrated area of the Ce^{3+} band and $\nu(\text{OH})$ vibration are easily disturbed in case of doped Ce-based solid solutions (i.e., CeZrO_x) where, depending on Ce content and its dispersion, only one of the two was meaningful. On the contrary, Ce M_5 -edge NEXAFS spectra were sensitive to Ce even with loading $\approx 5\%$, giving the technique access to all the possible combinations of Ce-based materials.

Supplementary Materials: The following supporting information can be downloaded at: <https://www.mdpi.com/article/10.3390/nano13020272/s1>. Table S1. Employed reactants quantities for the MOF synthesis. Table S2. Quantities of MOFs employed and quantities of oxides obtained after MOFs calcination. Table S3. Elemental composition, textural and structural properties of the six samples. ^a ICP results. ^b EDX results. Figure S1. Thermal protocol employed for (a) O_2 -TPO and (b) H_2 -TPR measurements. Figure S2. PXRD pattern of (a) C100-UiO-66 (red line), C50Z50-UiO-66 (green line) and C5Z95-UiO-66 (blue line) and (c) CeO_2 (red line), C50Z50 (green line) and C5Z95 (blue line). Detail of fcu and $Fm-3m$ main Bragg reflections are reported in panels (b,d), respectively. Figure S3. (a) C100, (b) C50Z50 and (c) C5Z95 PXRD experimental data (black line), refined pattern (red line) and difference function (blue line). Figure S4. N_2 adsorption/desorption isotherms of (a) C100-UiO-66 (red line), C50Z50-UiO-66 (green line) and C5Z95-UiO-66 (blue line) and (b) C100 (red line), C50Z50 (green line) and C5Z95 (blue line). Figure S5. FT-IR spectra collected on C100 during the: (a) protocol step I (temperature rises from black to green line), (b) O_2 -TPR (temperature rises from black to red line) and (c) H_2 -TPR (temperature rises from black to blue line). Detail of $\nu(\text{OH})$ and $\text{Ce}^{3+} {}^2F_{5/2} \rightarrow {}^2F_{7/2}$ electronic transition are reported in the smaller panels indicated with ' and ')', respectively. Figure S6. Examples of possible OH groups species potentially formed over CeO_2 and CeZrO_x surface. Ce^{4+} and Ce^{3+} atoms are represented with red and blue colours, respectively. Figure S7. FTIR spectra collected during H_2 -TPR experiment on (a–c) C50Z50 and (d–f) C5Z95 samples. Detail of (a,d) $\nu(\text{OH})$ and (b,e) $\text{Ce}^{3+} {}^2F_{5/2} \rightarrow {}^2F_{7/2}$ regions (temperature increases from black to blue line). (c) C50Z50 $\text{Ce}^{3+} {}^2F_{5/2} \rightarrow {}^2F_{7/2}$ integrated area (black squares) respect to temperature evolution (red squares). (f) C5Z95 t-OH position (blue line) respect to temperature evolution (red squares). Figure S8. C100 (a,b) Ce M_5 edge NEXAFS spectra collected during H_2 -TPR experiment. Temperatures are reported in the graph legend. Figure S9. (a) Ce^{3+} concentration evaluated by Ce M_5 -edge NEXAFS fit reported with respect to the Ce^{3+} FT-IR band integrated area collected at the same temperature. Linear fit is reported with red line whilst its equation and the Pearson R value are reported in the graph. (b) Residual plot for the employed linear fit model. Figure S10. (a) C50Z50 and (b) C5Z95 Ce M_5 -edge NEXAFS spectra measured during heating under 50 mL/min H_2 :He (3:2). Temperature increases from black to blue line. References [51–55,67] are cited in supplementary materials.

Author Contributions: D.S.: Conceptualization, formal analysis, writing—original draft preparation; S.M. and G.D.: formal analysis, writing—review and editing; P.T. and S.B.: supervision, visualization, writing—review and editing; S.R.-B.: Conceptualization, supervision, visualization, formal analysis, writing—review and editing. All authors have read and agreed to the published version of the manuscript.

Funding: This work was partially funded by the Margarita Salas grant financed by the Ministerio de Universidades, Spain, and by the European Union-Next Generation EU and also by the European Union's Horizon 2020 research and innovation program under grant agreement 837733.

Data Availability Statement: Not applicable.

Acknowledgments: The authors are grateful to APE-HE beamline (Elettra Synchrotron) for beamtime allocation and the experimental support. A. Kudinov is acknowledged for support with sample synthesis and characterization. M. Signorile is acknowledged for support during NEXAFS measurements and further scientific discussions. A. Kudinov and M. R. Salazar are acknowledged for support during NEXAFS spectra measurement. D. Simonne is acknowledged for support with NEXAFS data analysis.

Maria Carmen Valsania is acknowledged for TEM measurements. S. Rojas-Buzo acknowledges the Margarita Salas grant financed by the Ministerio de Universidades, Spain, and also funded by the European Union-Next Generation EU. This work has been partially performed in the framework of the Nanoscience Foundry and Fine Analysis (NFFA-MIUR Italy Progetti Internazionali) project.

Conflicts of Interest: The authors declare no conflict of interest. The funders had no role in the design of the study; in the collection, analyses, or interpretation of data; in the writing of the manuscript; or in the decision to publish the results.

References

1. Montini, T.; Melchionna, M.; Monai, M.; Fornasiero, P. Fundamentals and Catalytic Applications of CeO₂-Based Materials. *Chem. Rev.* **2016**, *116*, 5987–6041. [[CrossRef](#)] [[PubMed](#)]
2. Wang, F.; Wei, M.; Evans, D.G.; Duan, X. CeO₂-Based Heterogeneous Catalysts toward Catalytic Conversion of CO₂. *J. Mater. Chem. A* **2016**, *4*, 5773–5783. [[CrossRef](#)]
3. Ebrahimi, P.; Kumar, A.; Khraisheh, M. A Review of CeO₂ Supported Catalysts for CO₂ Reduction to CO through the Reverse Water Gas Shift Reaction. *Catalysts* **2022**, *12*, 1101. [[CrossRef](#)]
4. Yang, W.; Wang, X.; Song, S.; Zhang, H. Syntheses and Applications of Noble-Metal-Free CeO₂-Based Mixed-Oxide Nanocatalysts. *Chem* **2019**, *5*, 1743–1774. [[CrossRef](#)]
5. Paier, J.; Penschke, C.; Sauer, J. Oxygen Defects and Surface Chemistry of Ceria: Quantum Chemical Studies Compared to Experiment. *Chem. Rev.* **2013**, *113*, 3949–3985. [[CrossRef](#)]
6. Boaro, M.; Colussi, S.; Trovarelli, A. Ceria-Based Materials in Hydrogenation and Reforming Reactions for CO₂ Valorization. *Front. Chem.* **2019**, *7*, 28. [[CrossRef](#)]
7. Chang, K.; Zhang, H.; Cheng, M.J.; Lu, Q. Application of Ceria in CO₂ Conversion Catalysis. *ACS Catal.* **2020**, *10*, 613–631. [[CrossRef](#)]
8. Kim, H.J.; Jang, M.G.; Shin, D.; Han, J.W. Design of Ceria Catalysts for Low-Temperature CO Oxidation. *ChemCatChem* **2020**, *12*, 11–26. [[CrossRef](#)]
9. Chen, D.; Niakolas, D.K.; Papaefthimiou, V.; Ioannidou, E.; Neophytides, S.G.; Zafeiratos, S. How the Surface State of Nickel/Gadolinium-Doped Ceria Cathodes Influences the Electrochemical Performance in Direct CO₂ Electrolysis. *J. Catal.* **2021**, *404*, 518–528. [[CrossRef](#)]
10. Can, F.; Berland, S.; Royer, S.; Courtois, X.; Duprez, D. Composition-Dependent Performance of Ce_xZr_{1-x}O₂ Mixed-Oxide-Supported WO₃ Catalysts for the NO_x Storage Reduction-Selective Catalytic Reduction Coupled Process. *ACS Catal.* **2013**, *3*, 1120–1132. [[CrossRef](#)]
11. Wu, Z.; Li, M.; Howe, J.; Meyer, H.M.; Overbury, S.H. Probing Defect Sites on CeO₂ Nanocrystals with Well-Defined Surface Planes by Raman Spectroscopy and O₂ Adsorption. *Langmuir* **2010**, *26*, 16595–16606. [[CrossRef](#)] [[PubMed](#)]
12. Yang, C.; Lu, Y.; Zhang, L.; Kong, Z.; Yang, T.; Tao, L.; Zou, Y.; Wang, S. Defect Engineering on CeO₂-Based Catalysts for Heterogeneous Catalytic Applications. *Small Struct.* **2021**, *2*, 2100058. [[CrossRef](#)]
13. Konsolakis, M. Facet-Dependent Reactivity of Ceria Nanoparticles Exemplified. *Catalysts* **2021**, *11*, 452. [[CrossRef](#)]
14. Bozon-Verduraz, F.; Bensalem, A. IR Studies of Cerium Dioxide: Influence of Impurities and Defects. *J. Chem. Soc. Faraday Trans.* **1994**, *90*, 653–657. [[CrossRef](#)]
15. Kurajica, S.; Mužina, K.; Dražić, G.; Matijašić, G.; Duplančić, M.; Mandić, V.; Župančić, M.; Munda, I.K. A Comparative Study of Hydrothermally Derived Mn, Fe, Co, Ni, Cu and Zn Doped Ceria Nanocatalysts. *Mater. Chem. Phys.* **2020**, *244*, 122689. [[CrossRef](#)]
16. Xiong, Y.; Li, L.; Zhang, L.; Cao, Y.; Yu, S.; Tang, C.; Dong, L. Migration of Copper Species in Ce_xCu_{1-x}O₂ Catalyst Driven by Thermal Treatment and the Effect on CO Oxidation. *Phys. Chem. Chem. Phys.* **2017**, *19*, 21840–21847. [[CrossRef](#)]
17. Shan, W.; Luo, M.; Ying, P.; Shen, W.; Li, C. Reduction Property and Catalytic Activity of Ce_{1-x}Ni_xO₂ Mixed Oxide Catalysts for CH₄ Oxidation. *Appl. Catal. A Gen.* **2003**, *246*, 1–9. [[CrossRef](#)]
18. Barreau, M.; Chen, D.; Zhang, J.; Papaefthimiou, V.; Petit, C.; Salusso, D.; Borfecchia, E.; Turczyniak-Surdacka, S.; Sobczak, K.; Mauri, S.; et al. Synthesis of Ni-Doped Ceria Nanoparticles and Their Unusual Surface Reduction in Hydrogen. *Mater. Today Chem.* **2022**, *26*, 101011. [[CrossRef](#)]
19. Sher, M.; Javed, M.; Shahid, S.; Hakami, O.; Qamar, M.A.; Iqbal, S.; AL-Anazy, M.M.; Baghdadi, H.B. Designing of Highly Active G-C₃N₄/Sn Doped ZnO Heterostructure as a Photocatalyst for the Disinfection and Degradation of the Organic Pollutants under Visible Light Irradiation. *J. Photochem. Photobiol. A Chem.* **2021**, *418*, 113393. [[CrossRef](#)]
20. Li, Y.; Han, W.; Wang, R.; Weng, L.T.; Serrano-Lotina, A.; Bañares, M.A.; Wang, Q.; Yeung, K.L. Performance of an Aliovalent-Substituted CoCeO_x Catalyst from Bimetallic MOF for VOC Oxidation in Air. *Appl. Catal. B Environ.* **2020**, *275*, 119121. [[CrossRef](#)]
21. Nanoparticles, T.C.; Elias, J.S.; Risch, M.; Giordano, L.; Mansour, A.N.; Shao-horn, Y. Structure, Bonding, and Catalytic Activity of Monodisperse, Transition-Metal-Substituted CeO₂ Nanoparticles. *J. Am. Chem. Soc.* **2014**, *136*, 17193–17200.
22. Derafa, W.; Paloukis, F.; Mewafy, B.; Baaziz, W.; Ersen, O.; Petit, C.; Corbel, G.; Zafeiratos, S. Synthesis and Characterization of Nickel-Doped Ceria Nanoparticles with Improved Surface Reducibility. *RSC Adv.* **2018**, *8*, 40712–40719. [[CrossRef](#)]

23. Huang, J.; Li, W.; Wang, K.; Huang, J.; Liu, X.; Fu, D.; Li, Q.; Zhan, G. M XO Y-ZrO₂ (M = Zn, Co, Cu) Solid Solutions Derived from Schiff Base-Bridged UiO-66 Composites as High-Performance Catalysts for CO₂ Hydrogenation. *ACS Appl. Mater. Interfaces* **2019**, *11*, 33263–33272. [[CrossRef](#)]
24. Guo, Y.; Yu, Q.; Fang, H.; Wang, H.; Han, J.; Ge, Q.; Zhu, X. Ce-UiO-66 Derived CeO₂ Octahedron Catalysts for Efficient Ketoneization of Propionic Acid. *Ind. Eng. Chem. Res.* **2020**, *59*, 17269–17278. [[CrossRef](#)]
25. Fang, R.; Luque, R.; Li, Y. Efficient One-Pot Fructose to DFF Conversion Using Sulfonated Magnetically Separable MOF-Derived Fe₃O₄ (111) Catalysts. *Green Chem.* **2017**, *19*, 647–655. [[CrossRef](#)]
26. More, G.S.; Srivastava, R. Efficient Activation of CO₂ over Ce-MOF-Derived CeO₂ for the Synthesis of Cyclic Urea, Urethane, and Carbamate. *Ind. Eng. Chem. Res.* **2021**, *60*, 12492–12504. [[CrossRef](#)]
27. Mei, J.; Shen, Y.; Wang, Q.; Shen, Y.; Li, W.; Zhao, J.; Chen, J.; Zhang, S. Roles of Oxygen Species in Low-Temperature Catalytic o-Xylene Oxidation on MOF-Derived Bouquetlike CeO₂. *ACS Appl. Mater. Interfaces* **2022**, *14*, 35694–35703. [[CrossRef](#)]
28. Wang, Y.; Bi, F.; Wang, Y.; Jia, M.; Tao, X.; Jin, Y.; Zhang, X. MOF-Derived CeO₂ Supported Ag Catalysts for Toluene Oxidation: The Effect of Synthesis Method. *Mol. Catal.* **2021**, *515*, 111922. [[CrossRef](#)]
29. Sun, H.; Yu, X.; Ma, X.; Yang, X.; Lin, M.; Ge, M. MnOx-CeO₂ Catalyst Derived from Metal-Organic Frameworks for Toluene Oxidation. *Catal. Today* **2020**, *355*, 580–586. [[CrossRef](#)]
30. Bagi, S.; Yuan, S.; Rojas-Buzo, S.; Shao-Horn, Y.; Román-Leshkov, Y. A Continuous Flow Chemistry Approach for the Ultrafast and Low-Cost Synthesis of MOF-808. *Green Chem.* **2021**, *23*, 9982–9991. [[CrossRef](#)]
31. Wei, Y.S.; Zhang, M.; Zou, R.; Xu, Q. Metal-Organic Framework-Based Catalysts with Single Metal Sites. *Chem. Rev.* **2020**, *120*, 12089–12174. [[CrossRef](#)] [[PubMed](#)]
32. Cai, G.; Yan, P.; Zhang, L.; Zhou, H.-C.; Jiang, H.-L. Metal-Organic Framework-Based Hierarchically Porous Materials: Synthesis and Applications. *Chem. Rev.* **2021**, *121*, 12278–12326. [[CrossRef](#)] [[PubMed](#)]
33. Rojas-Buzo, S.; Concepción, P.; Olloqui-Sariego, J.L.; Moliner, M.; Corma, A. Metalloenzyme-Inspired Ce-MOF Catalyst for Oxidative Halogenation Reactions. *ACS Appl. Mater. Interfaces* **2021**, *13*, 31021–31030. [[CrossRef](#)] [[PubMed](#)]
34. Ding, M.; Cai, X.; Jiang, H.L. Improving MOF Stability: Approaches and Applications. *Chem. Sci.* **2019**, *10*, 10209–10230. [[CrossRef](#)] [[PubMed](#)]
35. Howarth, A.J.; Liu, Y.; Li, P.; Li, Z.; Wang, T.C.; Hupp, J.T.; Farha, O.K. Chemical, Thermal and Mechanical Stabilities of Metal-Organic Frameworks. *Nat. Rev. Mater.* **2016**, *1*, 15018. [[CrossRef](#)]
36. Garvie, L.A.J.; Buseck, P.R. Determination of Ce⁴⁺/Ce³⁺ in Electron-Beam-Damaged CeO₂ by Electron Energy-Loss Spectroscopy. *J. Phys. Chem. Solids* **1999**, *60*, 1943–1947. [[CrossRef](#)]
37. Livraghi, S.; Paganini, M.C.; Giamello, E.; Di Liberto, G.; Tosoni, S.; Pacchioni, G. Formation of Reversible Adducts by Adsorption of Oxygen on Ce-ZrO₂: An Unusual H₂ Ionic Superoxide. *J. Phys. Chem. C* **2019**, *123*, 27088–27096. [[CrossRef](#)]
38. Karnatak, R.C.; Esteva, J.M.; Dexpert, H.; Gasgnier, M.; Caro, P.E.; Albert, L. X-Ray Absorption Studies of CeO₂, PrO₂, and TbO₂. I. Manifestation of Localized and Extended f States in the 3d Absorption Spectra. *Phys. Rev. B* **1987**, *36*, 1745–1749. [[CrossRef](#)]
39. Paparazzo, E. Use and Mis-Use of x-Ray Photoemission Spectroscopy Ce3d Spectra of Ce₂O₃ and CeO₂. *J. Phys. Condens. Matter* **2018**, *30*, 343003. [[CrossRef](#)]
40. Rojas-Buzo, S.; Salusso, D.; Bonino, F.; Paganini, M.C.; Bordiga, S. Unraveling the Reversible Formation of Defective Ce³⁺ Sites in the UiO-66(Ce) Material: A Multi-Technique Study. *Mater. Today Chem.* **2023**, *27*, 101337. [[CrossRef](#)]
41. Laachir, A.; Perrichon, V.; Badri, A.; Lamotte, J.; Catherine, E.; Lavalley, J.C.; El Fallah, J.; Hilaire, L.; Le Normand, F.; Quéméré, E.; et al. Reduction of CeO₂ by Hydrogen. Magnetic Susceptibility and Fourier-Transform Infrared, Ultraviolet and X-Ray Photoelectron Spectroscopy Measurements. *J. Chem. Soc., Faraday Trans.* **1991**, *87*, 1601–1609. [[CrossRef](#)]
42. Vindigni, F.; Manzoli, M.; Tabakova, T.; Idakiev, V.; Boccuzzi, F.; Chiorino, A. Effect of Ceria Structural Properties on the Catalytic Activity of Au-CeO₂ Catalysts for WGS Reaction. *Phys. Chem. Chem. Phys.* **2013**, *15*, 13400–13408. [[CrossRef](#)]
43. Zhang, W.; Li, P.; Duan, X.; Liu, S.; Wang, Z. Enhanced Broadband Excitable Near-Infrared Luminescence in Ce³⁺/Yb³⁺ Codoped Oxyapatite Based Glass Ceramics. *Phys. B Condens. Matter* **2020**, *582*, 411898. [[CrossRef](#)]
44. Lin, J.; Su, Q. Luminescence and Energy Transfer of Rare-Earth-Metal Ions in Mg₂Y₈(SiO₄)₆O₂. *J. Mater. Chem.* **1995**, *5*, 1151–1154. [[CrossRef](#)]
45. Herrmann, A.; Othman, H.A.; Assadi, A.A.; Tiegel, M.; Kuhn, S.; Rüssel, C. Spectroscopic Properties of Cerium-Doped Aluminosilicate Glasses. *Opt. Mater. Express* **2015**, *5*, 720. [[CrossRef](#)]
46. Li, J.; Chen, L.; Hao, Z.; Zhang, X.; Zhang, L.; Luo, Y.; Zhang, J. Efficient Near-Infrared Downconversion and Energy Transfer Mechanism of Ce³⁺/Yb³⁺ Codoped Calcium Scandate Phosphor. *Inorg. Chem.* **2015**, *54*, 4806–4810. [[CrossRef](#)]
47. Binet, C.; Badri, A.; Lavalley, J.C. A Spectroscopic Characterization of the Reduction of Ceria from Electronic Transitions of Intrinsic Point Defects. *J. Phys. Chem.* **1994**, *98*, 6392–6398. [[CrossRef](#)]
48. Thomas, S.; Marie, O.; Bazin, P.; Lietti, L.; Visconti, C.G.; Corbetta, M.; Manenti, F.; Daturi, M. Modelling a Reactor Cell for Operando IR Studies: From Qualitative to Fully Quantitative Kinetic Investigations. *Catal. Today* **2017**, *283*, 176–184. [[CrossRef](#)]
49. Meunier, F.C.; Goguet, A.; Shekhtman, S.; Rooney, D.; Daly, H. A Modified Commercial DRIFTS Cell for Kinetically Relevant Operando Studies of Heterogeneous Catalytic Reactions. *Appl. Catal. A Gen.* **2008**, *340*, 196–202. [[CrossRef](#)]
50. Melián-Cabrera, I. Temperature Control in DRIFT Cells Used for: In Situ and Operando Studies: Where Do We Stand Today? *Phys. Chem. Chem. Phys.* **2020**, *22*, 26088–26092. [[CrossRef](#)]

51. Lammert, M.; Glißmann, C.; Stock, N. Tuning the Stability of Bimetallic Ce(IV)/Zr(IV)-Based MOFs with UiO-66 and MOF-808 Structures. *Dalt. Trans.* **2017**, *46*, 2425–2429. [[CrossRef](#)]
52. Rodríguez-Carvajal, J. Recent Developments of the Program Fullprof. *Newsl. Comm. Powder Diffr. IUCr* **2001**, *26*, 12–19.
53. Thompson, P.; Cox, D.E.; Hastings, J.B. Rietveld Refinement of Debye-Scherrer Synchrotron X-Ray Data from Al₂O₃. *J. Appl. Crystallogr.* **1987**, *20*, 79–83. [[CrossRef](#)]
54. Simonne, D.; Martini, A.; Signorile, M.; Piovano, A.; Braglia, L.; Torelli, P.; Borfecchia, E.; Ricchiardi, G. THORONDOR: Software for Fast Treatment and Analysis of Low-Energy XAS Data. *J. Synchrotron Radiat.* **2020**, *27*, 1741–1752. [[CrossRef](#)] [[PubMed](#)]
55. Ruckebusch, C.; Blanchet, L. Multivariate Curve Resolution: A Review of Advanced and Tailored Applications and Challenges. *Anal. Chim. Acta* **2013**, *765*, 28–36. [[CrossRef](#)] [[PubMed](#)]
56. Lammert, M.; Wharmby, M.T.; Smolders, S.; Bueken, B.; Lieb, A.; Lomachenko, K.A.; De Vos, D.; Stock, N. Cerium-Based Metal Organic Frameworks with UiO-66 Architecture: Synthesis, Properties and Redox Catalytic Activity. *Chem. Commun.* **2015**, *51*, 12578–12581. [[CrossRef](#)]
57. Shannon, R.D. Revised Effective Ionic Radii and Systematic Studies of Interatomic Distances in Halides and Chalcogenides. *Acta Crystallogr. Sect. A Found. Crystallogr.* **1976**, *32*, 751–767. [[CrossRef](#)]
58. Ronda-Lloret, M.; Pellicer-Carreño, I.; Grau-Atienza, A.; Boada, R.; Diaz-Moreno, S.; Narciso-Romero, J.; Serrano-Ruiz, J.C.; Sepúlveda-Escribano, A.; Ramos-Fernandez, E.V. Mixed-Valence Ce/Zr Metal-Organic Frameworks: Controlling the Oxidation State of Cerium in One-Pot Synthesis Approach. *Adv. Funct. Mater.* **2021**, *31*, 2102582. [[CrossRef](#)]
59. Libowitzky, E. Correlation of O-H Stretching Frequencies and O-H O Hydrogen Bond Lengths in Minerals. *Hydrog. Bond Res.* **1999**, *1059*, 103–115. [[CrossRef](#)]
60. Yang, Y.; Xia, Q.; Feng, M.; Zhang, P. Temperature Dependence of IR Absorption of OH Species in Clinopyroxene. *Am. Mineral.* **2010**, *95*, 1439–1443. [[CrossRef](#)]
61. Mayerhöfer, T.G.; Pipa, A.V.; Popp, J. Beer's Law—Why Integrated Absorbance Depends Linearly on Concentration. *ChemPhysChem* **2019**, *20*, 2748–2753. [[CrossRef](#)] [[PubMed](#)]
62. Badri, A.; Binet, C.; Lavalley, J.C. Use of Methanol as an IR Molecular Probe to Study the Surface of Polycrystalline Ceria. *J. Chem. Soc. Faraday Trans.* **1997**, *93*, 1159–1168. [[CrossRef](#)]
63. Deplano, G.; Signorile, M.; Crocellà, V.; Porcaro, N.G.; Atzori, C.; Solemsli, B.G.; Svelle, S.; Bordiga, S. Titration of Cu(I) Sites in Cu-ZSM-5 by Volumetric CO Adsorption. *ACS Appl. Mater. Interfaces* **2022**, *14*, 21059–21068. [[CrossRef](#)]
64. Menegazzo, F.; Manzoli, M.; Chiorino, A.; Boccuzzi, F.; Tabakova, T.; Signoretto, M.; Pinna, F.; Pernicone, N. Quantitative Determination of Gold Active Sites by Chemisorption and by Infrared Measurements of Adsorbed CO. *J. Catal.* **2006**, *237*, 431–434. [[CrossRef](#)]
65. Daturi, M.; Binet, C.; Lavalley, J.; Sporken, R. Surface Investigation on Ce_xZr_{1-x}O₂ Compounds. *Phys. Chem. Chem. Phys.* **1999**, *1*, 5717–5724. [[CrossRef](#)]
66. Kašpar, J.; Fornasiero, P.; Graziani, M. Use of CeO₂-Based Oxides in the Three-Way Catalysis. *Catal. Today* **1999**, *50*, 285–298. [[CrossRef](#)]
67. Ravel, B.; Newville, M. ATHENA, ARTEMIS, HEPHAESTUS: Data Analysis for X-ray Absorption Spectroscopy Using IFEFFIT. *J. Synchrotron Radiat.* **2005**, *12*, 537–541. [[CrossRef](#)] [[PubMed](#)]

Disclaimer/Publisher's Note: The statements, opinions and data contained in all publications are solely those of the individual author(s) and contributor(s) and not of MDPI and/or the editor(s). MDPI and/or the editor(s) disclaim responsibility for any injury to people or property resulting from any ideas, methods, instructions or products referred to in the content.